Method to map individual electromagnetic field components inside a photonic crystal

T. Denis,[1,*] B. Reijnders,[1] J. H. H. Lee,[1] P. J. M. van der Slot,[1] W. L. Vos,[2] and K.-J. Boller[1]

[1] *Laser Physics and Nonlinear Optics, MESA+ Institute for Nanotechnology, University of Twente, P.O.Box 217, 7500 AE Enschede, The Netherlands*
[2] *Complex Photonic Systems (COPS), MESA+ Institute for Nanotechnology, University of Twente, P.O.Box 217, 7500 AE Enschede, The Netherlands*
*t.denis@utwente.nl

Abstract: We present a method to map the absolute electromagnetic field strength *inside* photonic crystals. We apply the method to map the dominant electric field component E_z of a two-dimensional photonic crystal slab at microwave frequencies. The slab is placed between two mirrors to select Bloch standing waves and a subwavelength spherical scatterer is scanned inside the resulting resonator. The resonant Bloch frequencies shift depending on the electric field at the position of the scatterer. To map the electric field component E_z we measure the frequency shift in the reflection and transmission spectrum of the slab versus the scatterer position. Very good agreement is found between measurements and calculations without any adjustable parameters.

References and links

1. S. John, "Strong localization of photons in certain disordered dielectric superlattices," Phys. Rev. Lett. **58,** 2486–2489 (1987).
2. E. Yablonovitch, "Inhibited spontaneous emission in solid-state physics and electronics," Phys. Rev. Lett. **58,** 2059–2062 (1987).
3. J. D. Joannopoulos, S. G. Johnson, J. N. Winn, and R. D. Meade, *Photonic Crystals: Molding the Flow of Light* (Princeton University Press, 2008).
4. N. W. Ashcroft and N. D. Mermin, *Solid State Physics* (Holt, Rinehard & Winston, 1976).
5. R. Sprik, B. A. van Tiggelen, and A. Lagendijk, "Optical emission in periodic dielectrics," Europhys. Lett. **35,** 265–270 (1996).
6. P. Lodahl, A. F. van Driel, I. S. Nikolaev, A. Irman, K. Overgang, D. Vanmaekelbergh, and W. L. Vos, "Controlling the dynamics of spontaneous emission from quantum dots by photonic crystals," Nature **430,** 654–657 (2004).
7. M. Fujita, S. Takahashi, Y. Tanaka, T. Asano, and S. Noda, "Simultaneous inhibition and redistribution of spontaneous light emission in photonic crystals," Science **308,** 1296–1298 (2005).
8. H. Caglayan, I. Bulu, and E. Ozbay, "Highly directional enhanced radiation from sources embedded inside three-dimensional photonic crystals," Opt. Express **13,** 7645–7652 (2005).
9. A. F. Koenderink, M. Kafesaki, C. M. Soukoulis, and V. Sandoghdar, "Spontaneous emission in the near-field of two-dimensional photonic crystals," Opt. Lett. **30,** 3210–3212 (2005).
10. A. Rodenas, G. Zhou, D. Jaque, and M. Gu, "Rare-earth spontaneous emission control in three-dimensional lithium niobate photonic crystals," Adv. Mater. **21,** 3526-3530 (2009).

11. L. Sapienza, H. Thyrrestrup, S. Stobbe, P. D. Garcia, S. Smolka, and P. Lodahl, "Cavity quantum electrodynamics with Anderson-localized modes," Science **327,** 1352–1355 (2010).

12. M. R. Jorgensen, J. W. Galusha, and M. H. Bart, "Strongly modified spontaneous emission rates in Diamond-structured photonic crystals," Phys. Rev. Lett. **107,** 143902 (2011).

13. M. D. Leistikow, A. P. Mosk, E. Yeganegi, S. R. Huisman, A. Lagendijk, and W. L. Vos, "Inhibited spontaneous emission of quantum dots observed in a 3D photonic band gap," Phys. Rev. Lett. **107,** 193903 (2011).

14. T. Yoshie, A. Scherer, J. Hendrickson, G. Khitrova, H. M. Gibbs, G. Rupper, C. Ell, O. B. Shchekin, and D. G. Deppe, "Vacuum Rabi splitting with a single quantum dot in a photonic crystal nanocavity," Nature **432,** 200–203 (2004).

15. O. Painter, R. K. Lee, A. Scherer, A. Yariv, J. D. O'Brien, P. D. Dapkus, and I. Kim, "Two-dimensional photonic band-gap defect mode laser," Science **284,** 1819–1821 (1999).

16. H. - G. Park, S. - H. Kim, S. - H. Kwon, Y. - G. Ju, J. - K. Yang, J. - H. Baek, S. - B. Kim, and Y. - H. Lee, "Electrically driven single-cell photonic crystal laser," Science **305,** 1444–1447 (2004).

17. H. Altug, D. Englund, and J. Vuckovic, "Ultrafast photonic crystal nanocavity laser," Nature Phys. **2,** 484–488 (2006).

18. K. Nozaki, S. Kita, and T. Baba, "Room temperature continuous wave operation and controlled spontaneous emission in ultrasmall photonic crystal nanolaser," Opt. Express **15,** 7506–7514 (2007).

19. P. J. M. van der Slot, T. Denis, and K. - J. Boller, "The photonic FEL: toward a handheld THz FEL," in *Proc. of the FEL 2008,* V. Schaa, ed. (JACoW, 2008), pp. 231–234.

20. H. K. Park, J. R. Oh, and Y. R. Do, "2D SiN_x photonic crystal coated $Y_3Al_5O_{12} : Ce^{3+}$ ceramic plate phosphor for high-power white light-emitting diodes," Opt. Express **19,** 25593–25601 (2011).

21. M. Florescu, H. Lee, I. Puscasu, M. Pralle, L. Florescu, D. Z. Ting, and J. P. Dowling, "Improving solar cell efficiency using photonic band-gap materials," Sol. Energy Mater. Sol. Cells **91,** 1599–1610 (2007).

22. D. - H. Ko, J. R. Tumbleston, L. Zhang, S. Williams, J. M. DeSimone, R. Lopez, and E. T. Samulski, "Photonic crystal geometry for organic solar cells," Nano Lett. **9,** 2742–2746 (2009).

23. A. F. Oskooi, D. Roundy, M. Ibanescu, P. Bermel, J. D. Joannopoulos, and S. G. Johnson, "MEEP: A flexible free-software package for electromagnetic simulations by the FDTD method," Comput. Phys. Commun. **181,** 687–702 (2010).

24. A. F. Koenderink and W. L. Vos, "Optical properties of real photonic crystals: anomalous diffuse transmission," J. Opt. Soc. Am. B **22,** 1075–1084 (2005).

25. D. Englund and J. Vuckovic, "Direct analysis of photonic nanostructures," Opt. Express, **14,** 3472–3483 (2006).

26. U. K. Khankhoje, S. - H. Kim, B. C. Richards, J. Hendrickson, J. Sweet, J. D. Olitzky, G. Khitrova, H. M. Gibbs, and A. Scherer, "Modelling and fabrication of GaAs photonic-crystal cavities for cavity quantum electrodynamics," Nanotechnology **21,** 065202 (2010).

27. M. L. M. Balistreri, H. Gersen, J. P. Korterik, L. Kuipers, and N. F. van Hulst, "Tracking femtosecond laser pulses in space and time" Science **294,** 1080–1082 (2001).

28. S. I. Bozhevolnyi, V. S. Volkov, J. Arentoft, A. Boltasseva, T. Sondergaard, and M. Kristensen, "Direct mapping of light propagation in photonic crystal waveguides," Opt. Commun. **212,** 51-55 (2002).

29. L. Okamoto, M. Loncar, T. Yoshie, A. Scherer, Y. Qiu, and P. Gogna, "Near-field scanning optical microscopy of photonic crystal nanocavities," Appl. Phys. Lett. **82,** 1676-1678 (2003).

30. P. Kramper, M. Agio, C. M. Soukoulis, A. Birner, F. Müller, R. B. Wehrspohn, U. Gösele, and V. Sandoghdar, "Highly directional emission from photonic crystal waveguides of subwavelength width" Phys. Rev. Lett. **92,** 113903 (2004).

31. H. - H. Tao, R. - J. Liu, Z. - Y. Li, S. Feng, Y. - Z. Liu, C. Ren, B. - Y. Cheng, D. - Z. Zhang, H. - Q. Ma, L. - A. Wu, and Z. - B. Zhang, "Mapping of complex optical field patterns in multimode photonic crystal waveguides by near field scanning optical microscopy," Phys. Rev. B **74,** 205111 (2006).

32. M. Abashin, P. Tortora, I. Märki, U. Levy, W. Nakagawa, L. Vaccaro, H. Herzig, and Y. Fainman, "Near-field characterization of propagating optical modes in photonic crystal waveguides," Opt. Express **14,** 1643–1657 (2006).

33. S. Vignolini, F. Intonti, F. Riboli, D. S. Wiersma, L. Balet, L. H. Li, M. Francardi, A. Gerardino, A. Fiore, and M. Gurioli, "Polarization-sensitive near-field investigation of photonic crystal microcavities," Appl. Phys. Lett. **94,** 163102 (2009).

34. J. Dahdah, M. Pilar-Bernal, N. Courjal, G. Ulliac, and F. Baida, "Near-field observations of light confinement in a two dimensional lithium niobate photonic crystal cavity," J. Appl. Phys. **110,** 074318 (2011).

35. K. G. Lee, H. W. Kihm, J. E. Kihm, W. J. Choi, H. Kim, C. Ropers, D. J. Park, Y. C. Yoon, S. B. Choi, D. H. Woo, J. Kim, B. Lee, Q. H. Park, C. Lienau, and D. S. Kim, "Vector field microscopic imaging of light," Nat. Photonics **1,** 53–56 (2007).

36. M. A. Seo, A. J. L. Adam, J. H. Kang, J. W. Lee, S. C. Jeoung, Q. H. Park, P. C. M. Planken, and D. S. Kim, "Fourier-transform terahertz near-field imaging of one-dimensional slit arrays: mapping of electric-field-, magnetic-field-, and Poynting vectors," Opt. Express **15,** 11781–11789 (2007).

37. M. Schnell, A. Garcia-Etxarri, J. Alkorta, J. Aizpurua, and R. Hillenbrand, "Phase-resolved mapping of the near-field vector and polarization state in nanoscale antenna gaps," Nano Lett. **10,** 3524-3528 (2010).

38. E. Flück, N. F. van Hulst, W. L. Vos, and L. Kuipers, "Near-field optical investigation of three-dimensional photonic crystals," Phys. Rev. E **68,** 015601 (2003).
39. B. Hecht, H. Bielefeldt, Y. Inouye, D. W. Pohl, and L. Novotny, "Facts and artifacts in near-field optical microscopy," J. Appl. Phys. **81,** 2492–2498 (1997).
40. R. Carminati, A. Madrazo, M. Nieto-Vesperinas, and J. - J. Greffet, "Optical content and resolution of near-field optical images: Influence of the operating mode," J. Appl. Phys. **82,** 501–509 (1997).
41. P. J. Valle, J. - J. Greffet, and R. Carminati, "Optical contrast, topographic contrast and artifacts in illumination-mode scanning near-field optical microscopy," J. Appl. Phys. **86,** 648–656 (1999).
42. K. D. Weston and S. K. Buratto, "A reflection near-field scanning optical microscope technique for subwavelength resolution imaging of thin organic films," J. Phys. Chem. B **101,** 5684–5691 (1997).
43. D. C. Kohlgraf-Owens, S. Sukhov, and A. Dogariu, "Optical-force-induced artifacts in scanning probe microscopy," Opt. Lett. **36,** 4758–4760 (2011).
44. M. Labardi, S. Patane, and M. Allegrini, "Artifact-free near-field optical imaging by apertureless microscopy," Appl. Phys. Lett. **77,** 621–623 (2000).
45. M. Esslinger, J. Dorfmüller, W. Khunsin, R. Vogelgesang, and K. Kern, "Background-free imaging of plasmonic structures with cross-polarized apertureless scanning near-field optical microscopy," Rev. Sci. Instrum. **83,** 033704 (2012).
46. L. C. Maier, *Field Strength Measurements in Resonant Cavities* (Massachusetts Institute of Technology, 1949).
47. L. C. Maier and J. C. Slater, "Field strength measurements in resonant cavities," J. Appl. Phys., **23,** 68–77 (1952).
48. C. C. Johnson, *Field and Wave Electrodynamics* (McGraw-Hill, 1965).
49. R. A. Marsh, M. A. Shapiro, R. J. Temkin, V. A. Dolgashev, L. L. Laurent, J. R. Lewandowski, A. D. Yeremian, and S. G. Tantawi, "X-band photonic band-gap accelerator structure breakdown experiment," Phys. Rev. STAB **14,** 021301 (2011).
50. T. Denis, P. J. M. van der Slot, and K. - J. Boller, "Experimental design of a single beam photonic free-electron laser," in *Proc. of the FEL 2009*, S. Waller, ed. (JACoW, 2009), pp. 431–434.
51. Concerto V7.5, Cobham Ltd., UK, http://www.cobham.com
52. B. Guru and H. Hiziroglu, *Electromagnetc Field Theory and Fundamentals* (PWS Publishing Company, 1997).
53. H. Guo, Y. Carmel, W. R. Lou, L. Chen, J. Rodgers, D. K. Abe, A. Bromborsky, W. Destler, and V. Granatstein, "A novel highly accurate synthetic technique for determination of the dispersive characteristics in periodic slow wave circuits," IEEE Trans. Microwave Theory Tech. **40,** 2086–2094 (1992).
54. M. Kageshima, H. Jensenius, M. Dienwiebel, Y. Nakayama, H. Tokumoto, S. P. Jarvis, and T. H. Oosterkamp, "Noncontact atomic force microscopy in liquid environment with quartz tuning fork and carbon nanotube probe," Appl. Surf. Sci. **188,** 440–444 (2002).
55. M. Frimmer, Y. Chen, and A. F. Koenderink, "Scanning emitter lifetime imaging microscopy for spontaneous emission control," Phys. Rev. Lett. **107,** 123602 (2011).

1. Introduction

Photonic crystals attract a tremendous deal of interest as they offer to radically control the light propagation [1] and emission of light [2]. In photonic crystals the dielectric constant varies periodically on the order of the wavelength [3]. Due to this periodicity, the light propagates in the form of Bloch modes [3, 4]. An intriguing capability of photonic crystals is to shape the local radiative density of electromagnetic states (LDOS) inside the crystal , which is the key for controlling the interaction of light with matter [5]. Manipulating the LDOS allows, for example, the inhibition or the enhancement of spontaneous emission of embedded light sources [6-13]. This forms the basis for investigating the strong-coupling cavity regime in quantum electrodynamics [14]. Such manipulations also have far-reaching technological implications, such as the development of efficient micro scale lasers, LEDs or solar cells [15-22].

The field strength of the Bloch modes inside the photonic crystal at the locations of the emitters determine the local character of the LDOS [5]. Bloch mode fields of ideal photonic crystals, *i.e.*, assuming a perfect periodicity, can be calculated by numerical methods such as finite-difference time domain (FDTD) [23]. However, all real photonic crystals suffer inevitably from unpredictable non-periodic local deviations both due to fabrication errors and, also fundamentally, due to thermodynamical arguments [4, 24]. While interesting steps have been presented towards including such deviations by using two-dimensional scanning electron microscope images, complete three-dimensional deviations cannot be effectively included into numerical calculations [25, 26]. A measurement is the only way to analyze the electromag-

netic field inside a real photonic crystal. To eventually also characterize the LDOS of photonic crystals the field measurement method should resolve the direction and absolute value of the individual field components (E_x, E_y, E_z, H_x, H_y, H_z). A method to measure the absolute field strength of an eigenmode *inside* a real photonic crystal, however, has not been reported to date.

So far the only optical method to map local fields is near-field scanning optical microscopy (NSOM) [27-45].The technique relies on scanning a small tip of a tapered optical fiber *above* the surface of a photonic crystal that collects part of the evanescent field with subwavelength resolution. However, NSOM suffers from several drawbacks. First, while the method has been used to measure individual field components [35-37] it is restricted to probe local fields *outside* the crystal near its surfaces while the field deep *inside* the crystal cannot be mapped. Thus one needs to make assumptions about the scattering from the internal fields under study to the detected evanescent fields. In case of three-dimensional crystals, relating the fields at the surface to the derived fields in the bulk is even more challenging [38] than in the widely studied two-dimensional slab systems. Second, NSOM measurements are strongly affected by a number of background effects [39-43] making absolute field measurements very difficult. Even in most sophisticated NSOM methods which provide nearly background free detection schemes absolute fields have not been reported [44, 45]. What is desirable is to devise a method that can probe the absolute strength of the electromagnetic field *inside* a photonic crystal.

Here we demonstrate a method to measure the absolute strength of the electromagnetic field distribution *inside* a photonic crystal. Our method relies on measuring the resonant frequencies of Bloch standing waves in a photonic crystal of finite length that is enclosed by two mirrors. A subwavelength scatterer placed inside the crystal scatters the electromagnetic field which shifts the frequency of the Bloch resonances proportionally to the square of the electric and magnetic field strength at the scatterer position [46-49]. By measuring the frequency shifts as a function of the spatial position of the scatterer, we obtain maps of the field strengths versus position. We demonstrate the method at microwave frequencies where fabrication errors are relatively small. Furthermore, in this frequency range the typical structure sizes are sufficiently large that a scatterer can be conveniently scanned through the crystal. To simplify the demonstration we deliberately choose a photonic crystal design where a single field component inside the microwave photonic crystal slab dominates throughout most of the crystal. Using a spherical, metallic bead as a scatterer we thus map the dominant electric field component E_z *inside* a photonic crystal slab.

2. Measurement method

To map the electromagnetic field, a photonic crystal is placed between two mirrors. The mirrors restrict the electromagnetic field in the photonic crystal to discrete longitudinal Bloch modes with associated resonance frequencies v_0 and wave numbers k_z. To measure the electromagnetic field we place a scatterer inside the photonic crystal and measure the shift of the resonance frequencies. We chose a scatterer in the Rayleigh regime with a small size parameter $x \ll 1$, with $x = 2\pi R/\lambda$. Here, R is the radius of the object and λ the wavelength. In this regime the field is approximately constant throughout the scatterer volume, thereby the scattering can be treated within the electrostatic approximation to calculate the resulting frequency shift Δv due to the scatterer. Using a spherical metallic scatterer with a radius R we obtain [46-48].

$$\Delta v(\mathbf{r}) = \frac{\frac{1}{2}\mu_0 \mathbf{H}(\mathbf{r})^2 - \varepsilon_0 \mathbf{E}(\mathbf{r})^2}{U} \pi R^3 v_0 \tag{1}$$

where $\mathbf{E}(\mathbf{r})$ and $\mathbf{H}(\mathbf{r})$ are the unperturbed electric and magnetic fields at the location $\mathbf{r}$ of the scatterer, respectively. U is the total energy stored inside the unperturbed cavity, ε_0 is the permittivity and μ_0 the permeability of free space. If we measure the frequency shift versus the
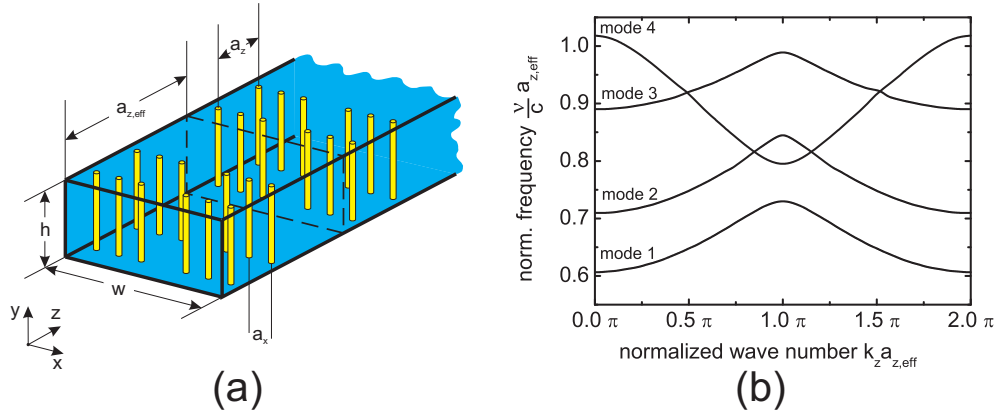
Fig. 1. (a) Schematic three-dimensional view of the photonic crystal slab indicating the defining geometry parameters. Metallic rods are placed inside a rectangular metallic waveguide. The dashed line indicates the size of the supercell. (b) Calculated band structure of the photonic crystal slab showing the four lowest TE-like modes having a non-zero E_z component of the electric field.

scatterer location $\Delta v(\mathbf{r})$ we will map, in a general photonic crystal, the electromagnetic field quantity $\left(\frac{1}{2}\mu_0\mathbf{H}(\mathbf{r})^2 - \varepsilon_0\mathbf{E}(\mathbf{r})^2\right)$.

In certain photonic crystal geometries, however, certain field components can strongly dominate, hence only these field components are mapped by using a spherical scatterer. For instance, in the crystal we use here, the E_z field dominates, $i.e.$, the E_z field strength is much greater than all other field components and the frequency shift becomes

$$\Delta v(\mathbf{r}) \approx -\frac{\varepsilon_0 E_z(\mathbf{r})^2}{U}\pi R^3 v_0 \tag{2}$$

Solving for the E_z component yields

$$E_z(\mathbf{r}) = \sqrt{\frac{-\Delta v(\mathbf{r})U}{\pi R^3 \varepsilon_0 v_0}}. \tag{3}$$

Equation (3) shows that it is possible to map the absolute strength of the E_z field component by measuring the frequency shift of the longitudinal resonances Δv versus the bead position and by determining the total energy stored in the cavity U for a specific input power P_{in}.

3. The photonic crystal slab

The unit cell of the photonic crystal slab we used (Fig. 1(a)) is designed to provide a dominant E_z component in the structure, which is also required for its intended application in a photonic free-electron laser [50]. The unit cell is a supercell which is surrounded by a metallic waveguide creating a two dimensional photonic crystal slab. A rectangular lattice of metal rods with a central line defect at $x = 0$ forms the basis of the supercell. Along the z-direction the rectangular lattice has a lattice constant of $a_z = 7.5\,$mm and the lattice constant is $a_x = 6.75\,$mm along the x-direction. Inside the supercell the third transverse row of rods is missing. Thus the supercell consists of 12 rods and has a length of $a_{z,\text{eff}} = 22.5\,$mm, indicated in Fig. 1(a). The diameter of the rods is 4 mm and the surrounding waveguide has a width of $w = 47.25\,$mm and a height of $h = 20\,$mm.
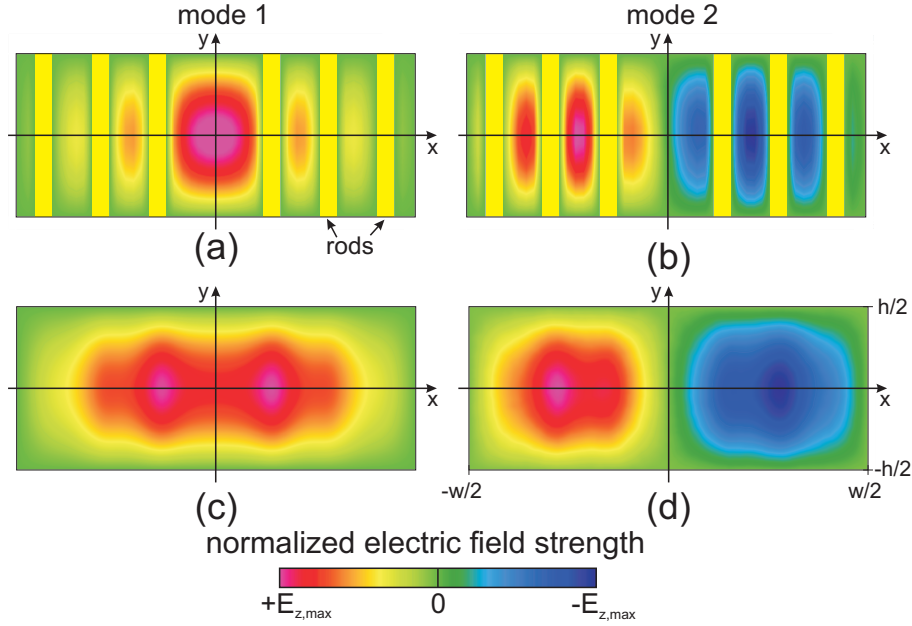
Fig. 2. Transverse E_z-eigenmode patterns of the photonic crystal slab for mode 1 and mode 2 at two cross sections (xy-plane) inside the unit cell. First, through the first row of rods (at $z = 0.5a_z$, (a) and (b)). Second, at a cross section through the empty part of the waveguide (at $z = 2.5a_z$, (c) and (d)). The normalized wave number for both patterns is $k_z a_{z,\text{eff}} = 0$ and the corresponding normalized frequency for (a) is 0.61 and for (b) 0.71.

To calculate the band structure of the photonic crystal slab a FDTD method is used [51]. In the calculations the photonic crystal slab is taken to be infinitely long along the z-direction by applying appropriate periodic boundary conditions to the unit cell. All metal parts are treated as perfect electric conductors which is well justified in the microwave range. Figure 1(b) shows the results for the four lowest-frequency TE-like modes, *i.e.*, modes with a non-zero longitudinal electric field component E_z. Due to the z-periodicity of the slab, the dispersion in the first Brillouin zone, *i.e.*, for normalized wave numbers ($a_{z,\text{eff}} k_z$) between 0 and 2π, repeats with increasing wave number [3]. Furthermore, the finite transverse size of the waveguide results in a lowest allowed normalized frequency of 0.61 for mode 1. No other TE-like modes exist below this cut-off frequency.

For a comparison with experimental field mapping data we calculate the local E_z field distribution of mode 1 and mode 2. The FDTD method is applied at the resonant frequency of mode 1 and 2 for a normalized wave number of $a_{z,\text{eff}} k_z = 0$ which corresponds to a normalized frequency of 0.61 and 0.71 respectively. Figure 2(a) through 2(d) show the E_z field pattern of the modes at two transverse planes at different z coordinates. The first plane is taken through the center of the first row of rods ($z = 0.5a_z$) and the second plane is taken in the empty row of the unit cell ($z = 2.5a_z$) where mapping is performed. As expected, the field pattern is symmetric due to the symmetry of the photonic crystal slab. Furthermore, throughout all field patterns it is observed that mode 2 has a field node at the center of the waveguide which will explain a certain effect in the experimental data later on.
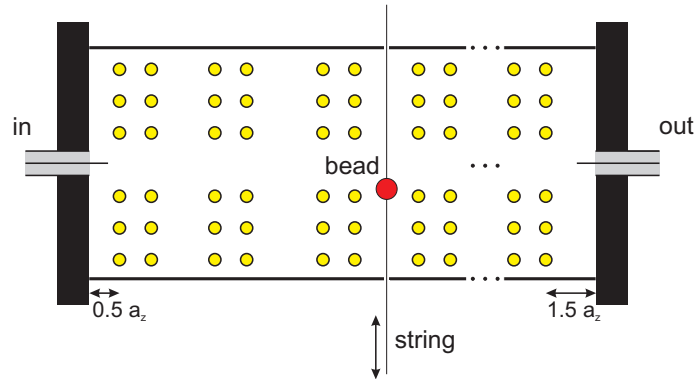
Fig. 3. Schematic view of the setup to measure the electromagnetic field inside the photonic crystal slab by a scatterer. The Fig. shows a cross section through the photonic crystal slab at $y = 0$. The photonic crystal slab is sandwiched between two aluminum mirrors (bold black). The input and output antennas are mounted at the center of both mirrors. To map the E_z field component along the x-direction a spherical metallic scatterer, which is mounted on a string, can be moved throughout the photonic crystal slab.

4. Experimental setup

A schematic view of the experimental setup is shown in Fig. 3. The photonic crystal, described in section 3, is placed between two highly reflective alumimun mirrors to form a resonator. The longitudinal resonator contains 15 unit cells of the photonic crystal in total. The first mirror is positioned at a distance of $0.5a_z$ from the center of the first row of rods and the second mirror is positioned at a distance of $1.5a_z$ from the last row of rods.

The photonic crystal slab is fabricated as follows. A channel with a rectangular cross section of $47.25 \, \text{mm} \times 20 \, \text{mm}$ is milled into a solid aluminum block (bottom plate) and is covered with an aluminum top plate. Both parts contain holes for mounting the rods. The rods are hollow brass cylinders with an inner diameter of $2 \, \text{mm}$ and an outer diameter of $4 \, \text{mm}$. With screws extending from the top plate through the rods into the bottom plate the rods are positioned. This also provides an electrical connection between the rods and the waveguide. The total positioning accuracy for the rods is estimated to a maximum of about $100 \, \mu \text{m}$, corresponding to a high precision of about 1.4% relative to the inter rod distances.

To measure the resonant frequencies of the photonic crystal slab cavity, a Hertzian dipole antenna [52] is mounted at the center of each mirror (see Fig. 3). Both antennas point along the $z-$direction to excite or detect modes with a non-zero E_z field component. One antenna acts as an emitter labeled "in" in Fig. 3 while the other antenna acts as a receiver for transmission measurements labeled "out" in Fig. 3. As a compromise between minimal loading of the resonator by the antennae and sufficient coupling to the modes, the length of both antennae was selected as $4 \, \text{mm}$. Note that with the antenna position in the center of the mirror, modes with an E_z field node in the center cannot be excited such as mode 2 shown in Fig. 2(c).

The other end of both antennae is connected to a network analyzer via coaxial SMA cables. The network analyzer is formed by a tunable microwave source with a maximum frequency of $20 \, \text{GHz}$ (Wiltron, model 69147A), two directional couplers (Krytar, model 2610) and two microwave power meters (Anritsu, model ML1438A with power heads MA2444A and MA2424B). To compensate for frequency dependent losses in cables and other components the network analyzer is calibrated before the measurements. The accuracy is estimated to about 10 %, as re-connecting coaxial cables typically has an effect in this magnitude. Using this setup

we measure the reflection and transmission spectra of the photonic crystal slab cavity. For the measurements the frequency resolution is set to 250 kHz and the input power P_{in} from the network analyzer is 1 mW.

To map the electromagnetic field inside the photonic crystal slab the scatterer is scanned through various locations inside the resonator. The scatterer is a stainless steel bead with a radius of $R = 2$ mm which sits on a 0.3 mm thick nylon string. As shown in Fig. 3 the string runs through two small holes (300 μm) in the opposing side walls. The holes are positioned in the center of the side walls ($y = 0$) and at $z = 2.5a_z$ inside the 3rd unit cell, as counted from the input side. At the position of the holes in the inner surface of the side walls a 4 mm deep cylindrical cavity with a diameter of 4.5 mm is fabricated in which the bead can fit completely. One end of the string is attached to a weight to keep the string straight via tension, and the other end of the string is mounted on a translation stage. The translation stage is used to position the bead with a relative accuracy of better than 0.05 mm. The absolute position is calibrated using the position at which the scatterer just completely disappears within the cylindrical cavity, and the error in this position is estimated to be smaller than 0.1 mm.

5. Dispersion measurement

Before measuring the E_z field component of the photonic crystal slab resonator we verified the appropriate description of the slab by the FDTD model. Specifically, to confirm the crystal dispersion we measured the resonance frequencies of the different longitudinal and transverse modes without a scatterer inside the photonic crystal. Measuring the dispersion is based on determining the longitudinal resonance frequencies of a finite-length photonic crystal consisting of n unit cells and assigning wave numbers to each observed resonance frequency [53]. For the assignment we consider the phase advance $\delta\phi$ of standing waves per round trip in the resonator. At each longitudinal resonance the phase advance per round trip along the z-direction is a multiple of π:

$$\delta\phi = na_{z,\text{eff}}k_z = m\pi \qquad m = 1, 2... \tag{4}$$

Here $na_{z,\text{eff}}$ is the geometrical length of the resonator and k_z is the wave number. As the resonator mirrors enclose 15 unit cells of the photonic crystal, $n = 15$ longitudinal resonances with a finite wavelength are expected [53] having a normalized wave number $a_{z,\text{eff}}k_z$ of

$$0 < a_{z,\text{eff}}k_z = \frac{m}{n}\pi \leq \pi. \tag{5}$$

From the calculations shown in Fig. 1(b) the frequency of the considered modes is seen to be a monotonously increasing or decreasing function of the wave number which renders the resonances denumerable. By using Eq. (5), a normalized wave number can be associated to each longitudinal resonance frequency, from which the dispersion of that transverse mode is obtained.

Figure 4 shows the measured transmission and reflection power spectrum of the unperturbed photonic crystal slab resonator in the range from 8 GHz to 14 GHz on a logarithmic power scale. For most of the measured frequencies the reflection is close to 0 dB meaning that it is equal to the input power of 1 mW. Due to the resonator a radiation field can only build up at frequencies where longitudinal resonances of a transverse photonic crystal mode exist. In both spectra we clearly observe the resonances belonging to the longitudinal resonances. As expected for such resonances the frequency of reflection and transmission resonances agree very well with each other.

By comparing the transmission levels of the various detected resonances we identify which resonance belongs to the same transverse mode. Four frequency ranges can be distinguished in
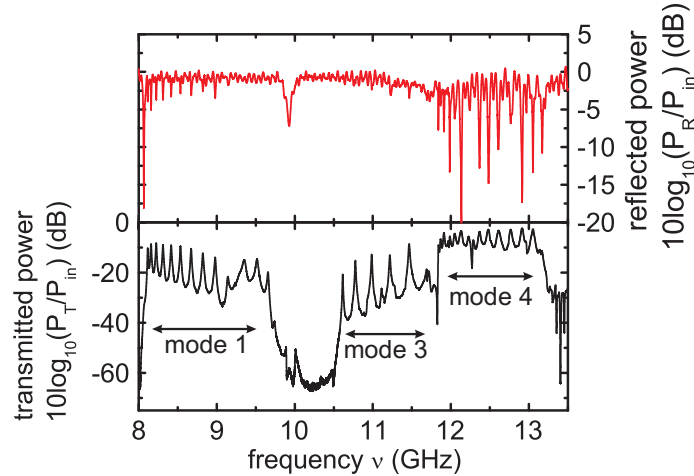
Fig. 4. Transmission and reflection spectrum of the photonic crystal slab without a scatterer between 8.0 GHz and 13.5 GHz. The peaks correspond to the various longitudinal modes for each transverse mode.

Fig. 4. From 8.0 GHz to 9.8 GHz sharp resonances appear with an averaged normalized transmission of about -15 dB. From 9.9 GHz to 10.7 GHz the transmission is very low (< -40 dB) and only one weak and broad resonance is observed. However, this is not a stop band of the slab, but a mode that cannot be effectively excited with a centered Hertzian dipole antenna due to its mode symmetry (Fig. 2). From 10.8 GHz to 11.8 GHz another set of resonances appears. This set of resonances is easily distinguished from the following set between 11.8 GHz to 13.3 GHz whose average transmission level (-10 dB) is much higher.

In total three different sets of resonances are identified as three different transverse modes. To retrieve the dispersion of each transverse mode we assign a wave number to the longitudinal resonances of each transverse mode. As an example for this process we concentrate on the frequency range from 8.0 GHz to 9.8 GHz. Fig. 5(a) shows a zoom into the reflection and transmission spectrum for this frequency range. For our photonic crystal slab of 15 unit cells, we expect from theory to observe 15 longitudinal resonances with a finite wavelength belonging to mode 1. Indeed, inspecting the transmission and reflection spectra, 15 resonances are observed. The first resonance is only clearly visible in the reflection spectrum. Furthermore, the resonances above the tenth one are only visible in the transmission spectrum due to a lower signal-to-noise ratio in the reflected signal.

Using these considerations we have used Eq. (5) to assign wave numbers to each measured resonance frequency of mode 1, as plotted in Fig. 5(b). The agreement with the theoretical dispersion (solid lines) is excellent. To assign also wave numbers to higher order modes we take into account, as was explained above, that mode 2 is not effectively excited with the centered Hertzian dipole antenna. Furthermore, the resonances of mode 4 can only be partly observed. Mode 4 overlaps in frequency with mode 3, but mode 3 couples better to the antenna as can be seen from the higher transmission level of mode 3. Hence, only mode 3 is detected where both modes overlap.

With these considerations we can assign normalized wave numbers to mode 3 and mode 4, as well. Also for these modes the agreement with the theoretical dispersion (solid lines) is excellent. In conclusion, the excellent agreement for mode 1 to mode 4 indicates an appropriate description of the fabricated slab with FDTD calculations.
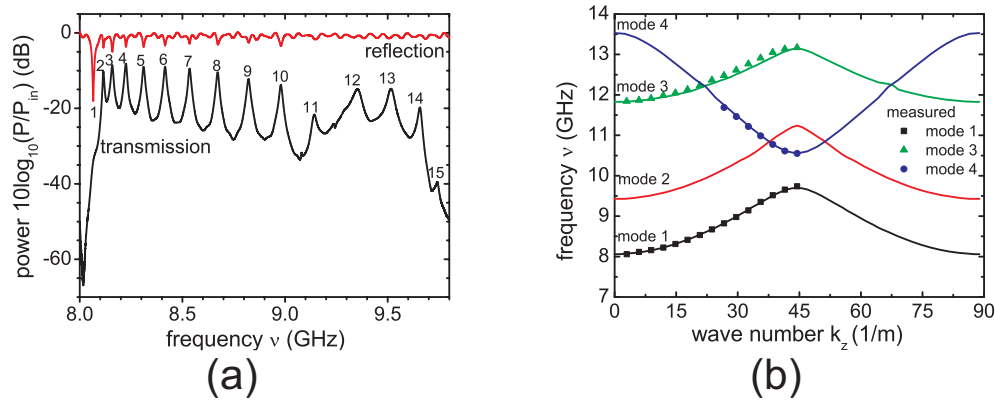
Fig. 5. (a) Zoom into transmission and reflection spectrum of the photonic crystal slab depicted in Fig. 4. The spectra clearly show the different longitudinal modes for transverse mode 1. The labeling depicts the number of anti-nodes, m, along the propagation direction. (b) Measured band structure of the photonic crystal slab for the four lowest frequency TE-like eigenmodes (symbols) compared to the calculated values from Fig. 1(b)

6. Electric field measurements

We measure the longitudinal electric field inside the photonic crystal slab by measuring the frequency shift of an individual longitudinal resonance due to a spherical metal scatterer inside the crystal. By scanning the position of the scatterer we can map the electric field distribution. Note that the measured frequency shift $\Delta\nu$ is referenced to the resonance frequency of the resonator loaded by the nylon string alone. The effect of the nylon string is small as it results in a shift of only 250 kHz.

Figure 6(a) and 6(b) show two examples of the measured frequency shift $\Delta\nu$ for mode 1 due to the scatterer. The frequencies of the two longitudinal resonances are 8.16 GHz and 8.42 GHz, respectively. The uncertainty of the frequency shift is 250 kHz due to the frequency resolution of the network analyzer. In both measurements the frequency shift remains always smaller or equal to zero, as we expect from Eq.(2) for a mode with a dominating E_z field component. Towards the edge of the waveguide the frequency shift $\Delta\nu$ approaches zero. As can be seen from Fig. 2, the electric field E_z is at these location close to zero and consequently also the frequency shift. The strongest frequency shift of about 4.75 MHz and 2.25 MHz, respectively, is reached in both examples at about 7.0 mm from the center. In between two rows of rods the strongest E_z field component along the x-direction is generally not located at the center of the waveguide but located slightly off the center, see Fig. 2.

To calculate the longitudinal electric field E_z from the measured frequency shift we apply Eq. (3). However, this requires to determine the total energy stored inside the cavity U. To retrieve U we use the definition of the quality factor:

$$Q = 2\pi\nu_0 \frac{U}{P_{diss}}. \qquad (6)$$

Exactly at resonance the dissipated power per cycle P_{diss} is equal to the input power P_{in} from the network analyzer. To retrieve the experimental Q-values we determine the full width half maximum of each transmission resonance ν_{FWHM} shown in Fig. 5(a) and use $Q = \nu_0/\nu_{FWHM}$.

Figure 6(c) and 6(d) show the resulting electric field strength E_z (square dots) determined for the two longitudinal resonances of mode 1 at a frequency of 8.16 GHz and 8.42 GHz, respectively. For a comparison, the figure displays also the E_z field strength from the FDTD
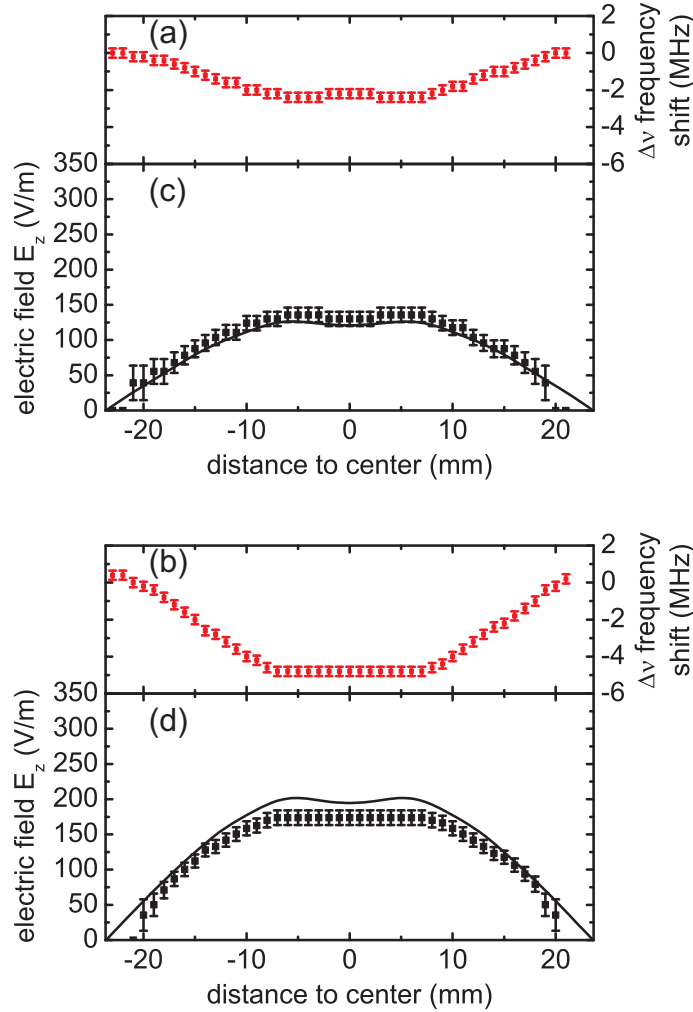
Fig. 6. Measured frequency shift $\Delta\nu$ induced by placing the spherical scatterer at that location for mode 1 at a longitudinal resonance frequencies of $\nu = 8.16\,\mathrm{GHz}$ (a) and $\nu = 8.42\,\mathrm{GHz}$ (b). The corresponding wave number is $k_z a_{z,\mathrm{eff}} = \frac{1}{15}\pi$ and $k_z a_{z,\mathrm{eff}} = \frac{6}{15}\pi$, respectively. The resulting electric field component E_z calculated from the measured frequency shift shown in (a) and (b) is shown in (c) and (d), respectively. The measured electric field component E_z (symbols) is compared to the calculated electric field (lines).

calculations presented in section 2 (black line). Uncertainties for the measured field values are determined by using the Gaussian error propagation law. We assume that the dominating errors are the uncertainty in input power of about 10 % and the frequency resolution of 250 kHz. All other uncertainties are much smaller and do not significantly contribute to the error bars of the measurement.

Figure 6(c) shows the results for a longitudinal resonance with a frequency of 8.16 GHz. The overall shape of the electric field shows an excellent agreement to the calculated field strength. Furthermore, also the absolute values agree within the range of the measurement accuracy, although no adjustable parameter is used in the calculations. Figure 6(d) shows an example at a higher frequency of 8.42 GHz. The agreement between FDTD calculations and experiment is

again very good. This holds both for the shape of the profile and also for the absolute values. Minor deviations are visible at the waveguide center. The small difference between electric field maximum and central electric field value at the center is calculated to be about 7 V/mm which is not resolved in the measurements. In addition, the measured absolute field value is slightly lower. We tentatively attribute both effects to the fact that at a higher frequency (shorter wavelength) influences due to non-periodic variations in the photonic crystal become more important. Nevertheless, in both examples a good agreement between experiment and theory is found.

The two discussed examples for mapping the electric field component E_z illustrate the capability of the method to map the absolute strength of an electric field component *inside* a photonic crystal. The good agreement between the measurements and calculations further clearly demonstrates that a field mapping *inside* a photonic crystal is possible.

7. Summary and outlook

We have demonstrated for the first time a method for mapping the absolute strength of an electromagnetic field component *inside* a photonic crystal. The method relies on measuring the change in resonance frequency when the photonic crystal is placed inside a resonator and the field inside the photonic crystal is perturbed by a sub-wavelength scatterer. A spherical scatterer is applied to measure the dominating longitudinal electric field E_z in a specific photonic crystal slab. We observe a good agreement between measured and calculated electric field strength E_z without using any adjustable parameters in the calculations.

Note that if all six field components would be of comparable strength, such as in an arbitrary photonic crystal or at specific locations, this measurement method can measure each individual field component by using a metallic needle instead of a metallic bead. The metallic needle short circuits and thus probes the electric field along the orientation of the needle while leaving all other field components unaffected. For a thin metallic needle with a thickness d and a length l aligned along the z-direction one obtains [46, 47]:

$$E_z(\mathbf{r}) = \sqrt{-12\frac{\Delta\nu(\mathbf{r})}{\nu_0}\frac{1}{\pi l^3}\frac{\ln(1+\sqrt{1-(d/l)^2})-\ln(1-\sqrt{1-(d/l)^2})-2\sqrt{1-(d/l)^2}}{(1-(d/l)^2)^{3/2}}} \quad (7)$$

In the future, this method could be applied in the near infrared or optical domain by scaling down the photonic crystal and the scatterer. Instead of a bead on a string we envision to mount a metallic or dielectric scatterer on one end of a stiff carbon nanotube whose other end is mounted to the tip of an atomic force microscope. The scatterer is then moved via moving the atomic force microscope tip. Mounting a carbon nanotube on an atomic force microscope has been demonstrated [54]. Further, atomic force microscopy allows a sufficiently high spatial resolution, demonstrated by recent measurements where an emitter directly mounted to an atomic force microscope has been used to map the emitter lifetime around a single nanorod [55]. Combining these results it should be possible to measure the shift in resonance frequency in the transmission spectrum to determine the absolute field strength inside air voids of an photonic crystal at optical frequencies.